

# Optical Cutting Tool Wear Monitoring by 3D Geometry Reconstruction

Rob Salaets<sup>1</sup>, Valentin Sturm<sup>2</sup>, Ted Ooijevaar<sup>3</sup>, Veronika Putz<sup>4</sup>, Julia Mayer<sup>5</sup> and Abdellatif Bey-Temsamani<sup>6</sup>

<sup>1,3,6</sup> *Flanders Make vzw, CoreLab DecisionS, Leuven, 3001, Belgium*  
*rob.salaets@flandersmake.be*  
*ted.ooijevaar@flandersmake.be*  
*abdellatif.bey-temsamani@flandersmake.be*

<sup>2,4,5</sup> *Linz Center of Mechatronics GmbH, Sensors & Communication, 4040 Linz, Austria*  
*valentin.sturm@lcm.at*  
*veronika.putz@lcm.at*  
*julia.mayer@lcm.at*

## ABSTRACT

Cutting tool wear needs to be monitored closely to ensure good quality of machined parts. However, manual inspection is both expensive and time consuming, therefore there is a need for automated monitoring methods. We present a technique that can reconstruct the cutting tool surface in 3D, allowing a spatial estimation of the tool wear with high accuracy. The reconstruction allows an automated direct monitoring method that estimates at any time the cutting tool condition, avoiding conversion work and major quality issues. The optical measurement setup consists of a hardware triggered line scan camera that registers the spinning cutting tool's shadow inflicted by a collimated backlight. We show how to leverage the 1D line scan signal acquired at varying cutting heights of the tool into a full 3D reconstruction. The progression of tool wear may thus be monitored by comparing the reconstructed shape to previous measurements. To this end we show a methodology for tool wear quantification. Additionally, to assess the measurement technique, an accuracy analysis with ground truth geometry was performed. The technique was applied to multiple degrading drilling tools. By automation of the cutting tool health monitoring, retrofitting this technology on a conventional machining center would transform it into an Industry 4.0 compatible (smart) machining center utilizing off-the-shelf optical equipment with moderate costs.

---

Rob Salaets et al. This is an open-access article distributed under the terms of the Creative Commons Attribution 3.0 United States License, which permits unrestricted use, distribution, and reproduction in any medium, provided the original author and source are credited.

## 1. INTRODUCTION

The wear of cutting tools is unavoidable in any cutting process, given the extreme levels of friction, stress and temperatures subjected to the tool. The relation of tool wear to part quality is evident: the dimensional accuracy and surface finish of the work piece are directly affected by a worn cutting tool. Furthermore, the degradation of cutting tools can occur unpredictably. This is the case when cutting composites, due to the composite laminates characteristics, such as inhomogeneity and anisotropy and to the layered structure and the extreme abrasiveness of fiber reinforcements (Bey-Temsamani, Ooijevaar, & Depraetere, 2019). Accordingly, there is a need for close monitoring of cutting tool wear, as a requirement for good quality of machined parts.

In this paper we investigate the feasibility of a 3D reconstruction of a rotating geometry using a single line scan camera for metrology purposes. We apply this with a particular focus on CNC cutting tools. Building on our previous research presented in (Bey-Temsamani et al., 2019), we propose a direct optical monitoring technique that can reliably detect tool wear based on periodic automated measurements. To this end, we use a line scan camera and collimated light to reconstruct the tool's geometry out of shadow scans of a spinning tool.

Cutting tool monitoring has been researched before, and is generally classified either direct or indirect monitoring. Direct methods try to assess measurements of the tool wear itself and indirect methods deduce the tool wear from sensor signals on the cutting machine implicitly.

In the field of indirect monitoring, multiple approaches exist. In (Krishnakumar, Rameshkumar, & Ramachandran, 2018) a feature based machine learning approach is proposed, where

multiple type of emissions, namely acoustic and vibration data are processed. The authors report high a classification efficiency. The authors of (Zhu & Zhang, 2019) propose a generic wear model which allows for prediction of milling force needed and remaining tool life.

A review on indirect methods can be found in (Kuntoğlu et al., 2020), where multiple articles are presented concerning monitoring schemes using vibration, heat and other emissions. Direct methods enable us to quantify the deviations or wear in a direct way. This can provide more insights than indirect monitoring, at the price of higher hardware costs. The wear can be spatially localized, allowing a classification of degradation processes. Furthermore, indirect methods are to be made robust to different cutting parameters, work piece materials and tool geometries, while direct methods do not have this requirement. In (Bagga, Makhesana, Patel, & Patel, 2021), the authors propose a direct method, namely a set-up with a camera and an image processing step to determine maximum flank wear measurement on CNC lathe machine. The authors of (Peng, Pang, Jiang, & Hu, 2020) use a similar setup. The resulting grayscale images are processed using software which allows the user to quantify tool wear. Both methods use machine vision techniques to analyse 2D images, but do not attempt a geometric reconstruction. The approach in the work of (Čerče, Pušavec, & Kopač, 2015) is most similar to ours, they use a 2D laser displacement sensor to measure the cutting tool surface. The approach also requires a motorized linear translation stage to displace the sensor over the static tool. In contrast, our approach leverages the mobility of the CNC machine tool and achieves similar repeatability with cheaper, more primitive camera technology.

In the industrial state of practice, the cutting tools are replaced preventively based on a visual inspection. This method has many limitations that makes it inefficient as a current practice. First, operators need to check the status of the cutting tool regularly by stopping the machine every now and then (Bey-Temsamani et al., 2019). A naked eye visual inspection can only be up to 100µm accurate, higher accuracies can be attained by taking the tool to a dedicated microscope. However, this is a lengthy and costly process.

Our proposed method allows the automation of cutting tool quality monitoring, because the measurement setup is in the machine tool working volume. A short (~ 30 seconds) measurement cycle can be executed after some CNC operations have been done, without stopping the machine. A comparison of measurements of a tool in pristine condition and after use, will reveal the amount of tool wear that has occurred. The simplicity of the optical setup allows for retrofitting existing CNC machining centres with ease.

The following section describes the optical setup and the necessary data acquisition modalities. Section 3 introduces the processing steps of the 3D reconstruction method. In Section

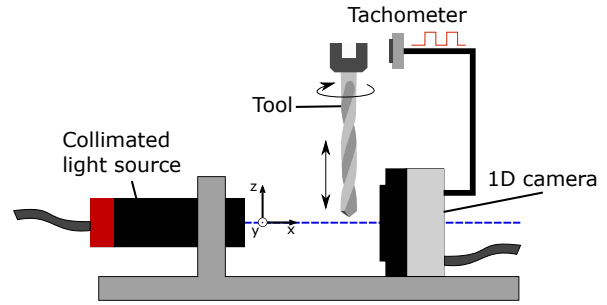


Figure 1. An schematic overview of the optical setup.

4 we analyse the accuracy and repeatability of our method. Section 5 presents the application of our method on a dataset of worn drilling tools. A concluding remark is made in Section 6.

## 2. OPTICAL SETUP AND DATA ACQUISITION

The hardware of the measurement setup consists of a line scan camera, a collimated light source and an optical tachometer. Figure 1 illustrates their arrangement. During measurement, the tool remains clamped in the spindle. The CNC machine places the tool between camera and light source, increments its vertical position in small steps and rotates the tool at the lowest rotational speed ( $\approx 3500$  rpm). The cutting tool is backlit using a collimated light source, which is placed at a distance of 140mm from the tool and 150 mm from the front face of the camera. To measure the actual rotation speed and to align the captured data with the angular orientation of the tool, an optical tachometer is used. It captures a white marking on a dark background fixed onto the clamping nut and outputs a triggering signal (a rectangular wave with a single rising edge at each revolution of the tool). The tachometer signal is used to trigger a monochromatic line scan camera (Basler Racer type raL2048-48gm, pixel size  $7\mu\text{m}$ , 2046 pixel/scan), which subsequently captures 2500 scan lines at a repetition rate of 50kHz at each rising edge. One frame is stored at each depth level together with the CNC coordinates from the controller. The camera speed and pixel size need to be chosen to match the requirements imposed by the minimal rotational speed of the spindle and the tool size respectively.

## 3. TOOL RECONSTRUCTION METHOD

### 3.1. Processing pipeline

The geometry reconstruction consists of multiple stages, they are depicted in Figure 2. For each vertical depth step a shadow trace of the spinning tool (line scan image) is recorded. Using a thresholding approach the shadow edge locations on the left and right side are accurately estimated, as described in Subsection 3.2. These signals contain some duplicated information, they can be aggregated to improve the estimates. Subsequently, the cross section of the tool can be reconstructed.

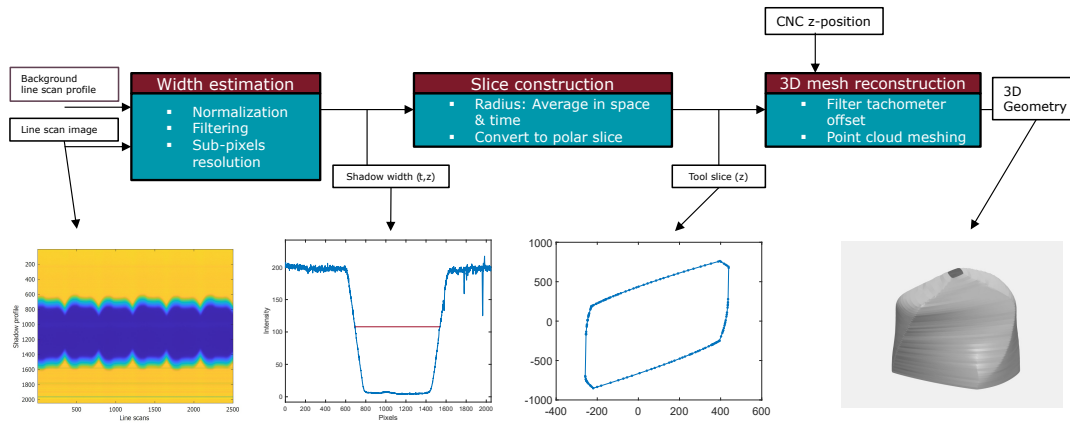


Figure 2. Overview of the 3D reconstruction pipeline.

These aspects are presented in Subsections 3.3 and 3.4. A point cloud can be obtained by stacking up the reconstructed cross sections. A straightforward meshing algorithm is introduced in Subsection 3.5.

### 3.2. Shadow width estimation

Figure 3, top left, shows raw data recorded from a helix-shaped cutting tool<sup>1</sup> at a fixed vertical position of the CNC machine as 2D image. The vertical axis displays intensity values recorded by the camera in a single scan as gray value. The horizontal axis shows all 2500 scanlines recorded from the rotating tool in a single experiment, i.e. data recorded while the tool performed three full rotations about 360°. Although a collimated light source was used, the transition from areas with low intensity (in which the light source was shadowed by the tool) and areas with high intensity (in which the sensor was directly illuminated by the light source) is soft, it covers a width of 0.63 mm. The soft shadow needs to be sampled sufficiently for accurate estimates, which requires a line scan camera with pixel size two orders of magnitude smaller (See Section 2). Due to the soft shadow effect, the relation between the width of the shadow created by the tool and the actual projected width is not straightforward. Especially in data recorded from the tip of the tool (which is highly relevant for measuring tool wear), the transition between illuminated and shadowed areas strongly influences the measurement. In this subsection, we present two thresholding techniques.

Besides the soft transition between bright areas and shadowed areas, as visible in Fig. 3, top left, also some sensitivity variations of the camera appear as horizontal lines. To account for these disturbances in a raw image  $I$ , the image was smoothed by applying a simple 2D-moving average filter

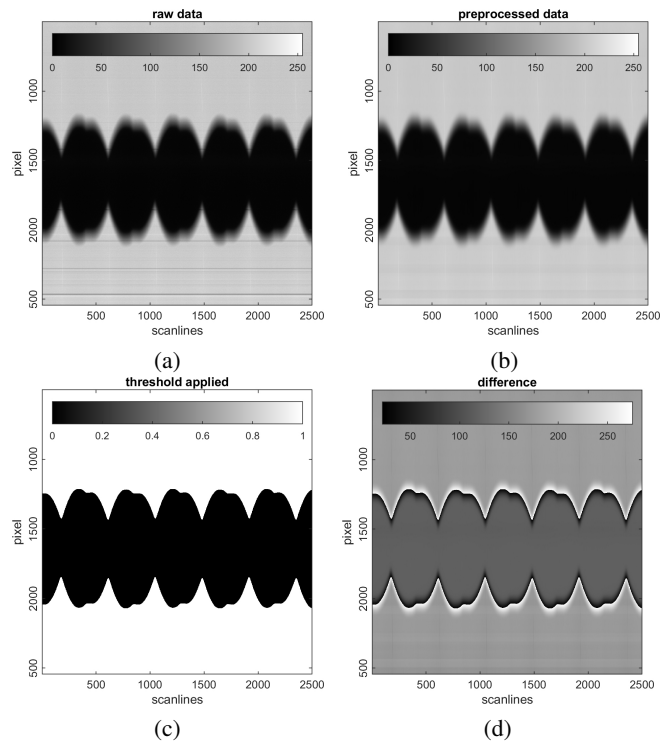


Figure 3. Line scan processing pipeline: The recorded raw data (a) is normalized, and sensitivity deviations of the used camera are compensated (b). A binary threshold is applied (c), and the deviation of the preprocessed data from the binarized image is further evaluated (d)

<sup>1</sup>Izartool 6,00 mm-DRILL BIT HSSE DIN338N

of length 61:

$$\hat{I}_{i,j} = \frac{1}{(\hat{k}_1 - \hat{k}_2 + 1)(\hat{l}_1 - \hat{l}_2 + 1)} \sum_{k_1=\hat{k}_{1,1}}^{\hat{k}_{1,2}} \sum_{k_2=\hat{k}_{1,1}}^{\hat{k}_{1,2}} I_{i+k_1, j+k_2},$$

with

$$\begin{aligned} \hat{k}_1(i) &:= \max\{-i + 1, 30\}, & \hat{k}_2(i) &:= \min\{n - i, 30\}, \\ \hat{l}_1(j) &:= \max\{-j + 1, 30\}, & \hat{l}_2(j) &:= \min\{n - j, 30\}. \end{aligned}$$

Figure 3, top right, shows our exemplary data after such a pre-processing step. Line scan images without the tool in front of the camera can serve as a background image which can be subtracted from the line scans with a tool present. This method works well when the noise is dominated by variations in pixel sensitivity.

**Adaptive threshold** The first thresholding method, denoted with  $M_a$ , rescales each scan line individually to contain values between 0 and 1, and applies a transformation afterwards of the form:

$$T(\hat{I}_{i,j}, th) := \begin{cases} 1 & \text{if } \hat{I}_{i,j} \geq th, \\ 0 & \text{if } \hat{I}_{i,j} < th. \end{cases}$$

The parameter  $th$  is determined for each scan line by minimizing the following error term

$$th(j) := \min \left\{ th_2, \underset{th \in R}{\operatorname{argmin}} \sum_{i=1}^{2046} |T(\hat{I}_{i,j}, th) - \hat{I}_{i,j}| \right\},$$

where  $th_2$  is introduced to reduce diameter- overestimation for small shadow widths. It was learned on a different dataset with a different drill, such that this algorithm minimized the overall reconstruction error with respect to mean absolute deviation. Figure 3, bottom left, shows the pre-processed data after applying a threshold using the function  $T$ . The deviation from this threshold is illustrated in Fig. 3, bottom right. After minimizing with respect to each scan line, we are able to extract the left and right shadow edge positions by taking the minimal and maximal position where the value is 1. These values are multiplied with the pixel size to return an estimate in  $\mu m$ .

**Fixed threshold** The fixed threshold method, denoted with  $M_f$ , compares normalized line scans to a single threshold intensity. It was empirically found that a threshold of halfway ( $th = 0.5$ ) between the darkest shadow intensity level and background intensity level is most robust to the influence of the tool position. The distance between the cutting tool and camera widens the shadow edge, as no light source is perfectly collimated. The shadow edges are now found by searching for the zero crossing points of  $\hat{I}_{i,j} - 0.5$ . This done by

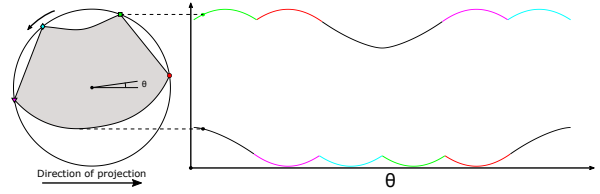


Figure 4. Illustration of shape projection and duplicated information in shadow edges.

calculating the analytical roots of a least-squares parabolic fit through the points around the indices where  $\hat{I}_{i,j} - 0.5$  changes sign. Note that the threshold was optimized for robustness, instead of the actual projection width of the tool. Therefore, the final shape reconstruction needs to be scaled by a scaling factor that minimizes the reconstruction error.

### 3.3. Filtering in time, space and phase

For each depth level, the shadow edges are registered during multiple rotations of the tool. Due to the collimated light, the shadow of the tool is an orthogonal projection on the line sensor of a planar cross section of the geometry, for the current depth level (See Figure 4).

The estimated shadow edge locations correspond to the extrema of the projected shape over a period of time. Both left and right edge locations ( $s_l[t]$ ,  $s_r[t]$ ) contain information of projected shape. This is depicted in Fig 4, it is clear that both the top and bottom traces of the shadow edge capture the same periodic pattern but inverted and phase shifted by a half revolution. For robustness against sensor noise the signals can be averaged over  $I$  periods with length  $T$ :

$$s_{avg}[t] = \frac{1}{I} \sum_{i=0}^{I-1} s[t + iT]$$

Afterwards a phase shifted average over left and right combines the information in both shadow edges. The result is a filtered half projection width:

$$h[t] = \frac{1}{2} (s_{r,avg}[t] - s_{l,avg}[\operatorname{circ}(t - T/2, T)])$$

Here  $\operatorname{circ}$  wraps around negative indices to the end of the array for a periodic extension. We estimate the period length  $T$  by finding the second local maximum of the cross-correlation function of  $s_r$  or  $s_l$  with a smaller subsection. A rough estimate of the spindle's angular velocity helps to identify the correct peak. When a speed controlled spindle is used, the angular velocity of tool can be regarded as constant, therefore the independent variable  $t$  can be regarded as the rotation angle, as shown in Figure 4.

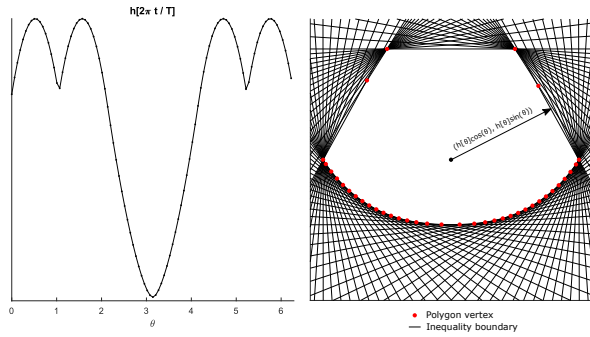


Figure 5. Illustration of duplicated information in shadow edges.

### 3.4. Slice reconstruction

The inverse problem at hand is similar to computed tomography. However, in this case we consider an opaque geometry instead of translucent imaging. Computed tomography methods result in a discretization of the two-dimensional space. Recognizing these important differences, we present an approach where the shape reconstruction is obtained by solving the vertex enumeration problem with a primal-dual polytope method (Bremner, Fukuda, & Marzetta, 1998). The vertex enumeration problem computes the vertices of the n-polytope that satisfies a set of inequalities. Figure 5 displays how the resulting convex polygon is constructed. The system of inequalities is given by:

$$\mathbf{Ax} \leq \mathbf{b}$$

With the rows of  $\mathbf{A}$  and elements of  $\mathbf{b}$  given by:

$$a_t = (\cos(2\pi t/T) \quad \sin(2\pi t/T)),$$

$$b_t = (h[t]), t = 0, \dots, T - 1$$

See (Bremner et al., 1998) for a detailed description of the primal-dual method for vertex enumeration. By projecting the shape onto the line sensor, information is lost. Indeed, only the convex hull of the shape can be reconstructed. However, convexity is only enforced in the two-dimensional cross section perpendicular to the axis of rotation. Vertical concavity can be present in the entire three-dimensional reconstruction. Depending on the application, that is an important limitation of the technique. We argue that for tool wear detection it is not a critical limitation, because tool wear occurs primarily at the convex ridges of the geometry (e.g. cutting edge and drill margin for drilling tools).

The acquisition of line scan frames is synchronised by a digital tachometer signal. However, we have observed a phase uncertainty with sample standard deviation  $\sigma \approx 1.25^\circ$ . This error would be a dominant factor of the total inaccuracy, but it can be reduced by filtering over all cross sections. Neighbouring cross sections have a similar shape and therefore the phase difference can be estimated with a circular cross correlation.

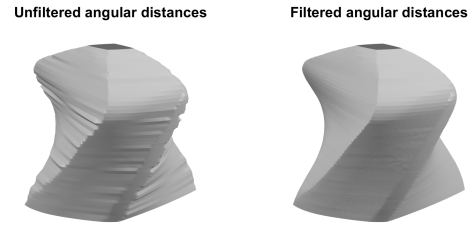


Figure 6. Illustration of the effect of filtering the angular distances.

The array of angular differences can be filtered to smooth out the noise. Filtering should not reduce the total angular twist of the tool, therefore a filtering technique should be applied with care. We employ a one-dimensional Laplacian smoothing (Lo, 1985). Let  $d[i]$  be the angular differences between two cross sections and  $s[i] = \sum_{k=0}^i d[k]$  for  $i = 0, \dots, I$ . The smoothing updates are given by:

$$s' = s - \lambda \mathbf{L}s$$

$$\mathbf{L} = \begin{pmatrix} -0.5 & 1 & -0.5 & & \\ & \ddots & \ddots & \ddots & \\ & & -0.5 & 1 & -0.5 \end{pmatrix}$$

where updates are applied multiple times on the inner points:  $i = 1, \dots, I - 1$ . We found that 20 iterations with  $\lambda = 0.8$  works well. The effect of this filtering is apparent in Figure 6.

### 3.5. Point cloud and mesh construction

Solving the vertex enumeration problem for each depth level results in a point cloud that can be meshed into a triangular surface. Because the points are effectively coming from a set of planer cross sections of the tool, this structure can be exploited for a simplified meshing method. The problem reduces to connecting the points of two subsequent cross sections into triangles. A good mesh has minimal skewness of the triangles. To this end, we employ the Dynamic Time Warp (DTW) transform on the points in cylindrical coordinates. The DTW finds the closest match between the lists of angular coordinates, the output consists of two monotonically increasing arrays of indices that contain a many-to-many mapping between indices. Multiplicity of a node results in duplicated indices in the list.

Listing 1 describes the meshing algorithm. Note that the point cloud is not altered, the output is merely a selection of triplets for a surface triangularization. The process is further illustrated in Figure 7, green triangles are created out of the black pairs that are outputted by the DTW transform.

**Data:**  $(r_i[k], \theta_i[k], z_i[k])$  cylindrical coordinates of the points of at every depth level  $i = 1, \dots, I$

**Result:**  $T$  the set of triangles

$T \leftarrow \emptyset$

**for**  $i=2$  **to**  $I$  **do**

$ia, ib \leftarrow \text{DynamicTimeWarp}(\theta_{i-1}[k], \theta_i[k])$

**for every pair**  $(a_k, b_k)$  **in**  $(ia, ib)$  **do**

**if**  $a_k == a_{k-1}$  **then**

      Append( $T, \text{GlobalIndex}(a_k, b_{k-1}, b_k)$ )

**else if**  $b_k == b_{k-1}$  **then**

      Append( $T, \text{GlobalIndex}(a_{k-1}, b_k, a_k)$ )

**else**

      Append( $T, \text{GlobalIndex}(a_{k-1}, b_{k-1}, b_k)$ )

      Append( $T, \text{GlobalIndex}(a_{k-1}, b_k, a_k)$ )

**end**

**end**

**end**

**Algorithm 1:** Triangle meshing algorithm. The *GlobalIndex* function maps three local indices to the global indices to be used in a connectivity matrix.

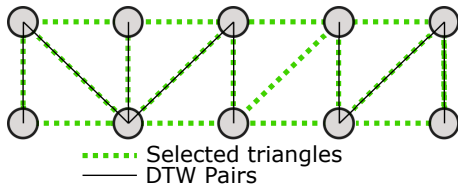


Figure 7. Illustration of the DTW meshing method.

## 4. ACCURACY ANALYSIS

### 4.1. Accuracy analysis of width estimation

In this section we present an accuracy analysis for our fixed threshold and adaptive threshold shadow width estimation methods, which were defined in Section 3. We recorded three measurements of the same tool, and in the following we compare the reconstructed shapes based on these three measurements with the ground truth. Afterwards, we discuss the repeatability by comparing our three different reconstructions with each other.

A ground truth geometry of the drill used for this analysis was obtained with a 3D scanner (GOM Atos Core 200). For structured light scanning of metal cutting tools an anti-reflective coating spray is needed. Considering these conditions an accuracy of 15-20 $\mu\text{m}$  can be expected. This puts a lower bound on our accuracy analysis.

For our first analysis, we considered a cross section at each z-level of our ground truth and compared it with the respective reconstruction. To this end, we randomly sampled points from the outlines and subtracted the estimated radius from the ground truth. The results thereof are depicted in two histograms in Figure 8 and Figure 9. We provide some performance measures, namely Mean Signed Difference (MSD), Mean Absolute Error (MAE), Root Mean Squared Error (RMSE) and 5%- and 95%-quantiles in Table 1.

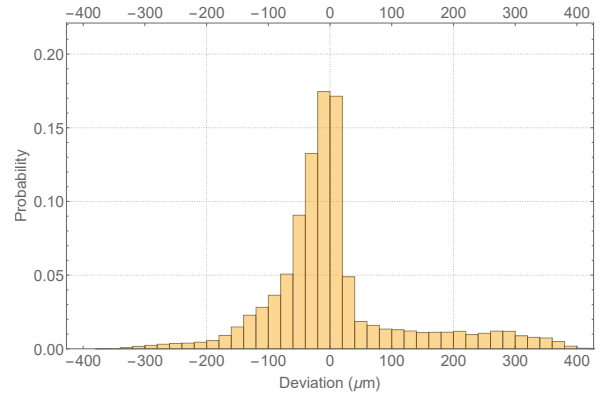


Figure 8. Histogram of deviation values in  $\mu\text{m}$  when reconstructing the shape with the adaptive threshold method  $M_a$ .

In Table 1 we can see that the first two average error met-

Table 1. Performance measures in  $\mu\text{m}$  for two considered approaches with respect to shape reconstruction

Approach	MSD	MAE	RMSE	$q_{0.05}$	$q_{0.95}$
$M_a$	7.85	72.70	111.98	-133.66	276.74
$M_f$	-12.40	73.71	107.68	-160.81	222.05

rics and the 5%-quantile values are more favorable for the  $M_a$  Method, while the 95%-quantile and the RMSE is better in case of applying the  $M_f$  reconstruction. In general, the results do not indicate a large difference in reconstruction quality.

For our second analysis, we analysed our three reconstructions by examining all three possible pairwise comparisons and averaged the results. Similar to our analysis before we also calculated some performance metrics in Table 2 below. When comparing Table 1 and 2 we can observe that the re-

Table 2. Performance Measures in  $\mu\text{m}$  for our two considered approaches with respect to repeatability.

Approach	MSD	MAE	RMSE	$q_{0.05}$	$q_{0.95}$
$M_a$	-0.507	5.697	8.163	-14.0	12.78
$M_f$	-0.741	4.416	6.291	-11.85	9.67

peatability error is one order of magnitude smaller than the reconstruction error for each respective metric. Moreover, it shows that with respect to repeatability the  $M_f$  Method performs superior, with better values than  $M_a$  for each performance measure except MSD. The resulting error distributions are depicted in Figure 10 and Figure 11.

### 4.2. Geometry alignment challenges

Some information is lost during the reconstruction, i.e. the convex hull of a cross section can be reconstructed (Subsection 3.4). This makes the comparison with a ground truth

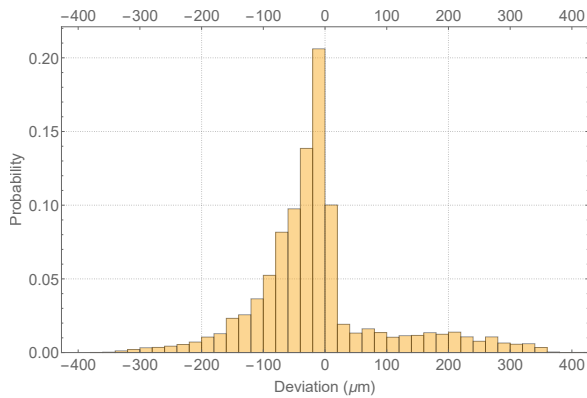


Figure 9. Histogram of deviation values in  $\mu m$  when reconstructing the shape with the fixed threshold method  $M_a$ .

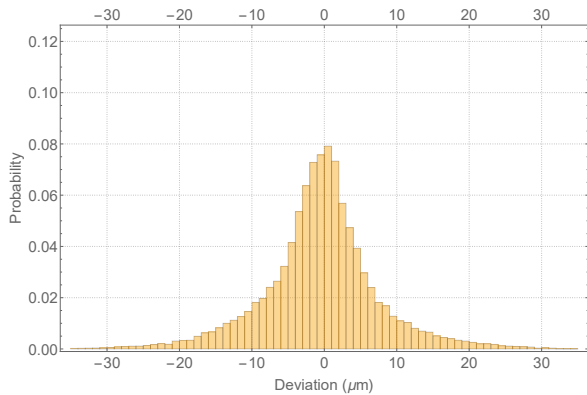


Figure 10. Repeatability error of reconstructions using method  $M_a$ .

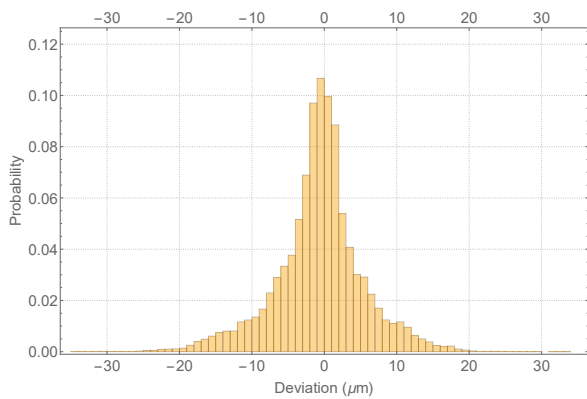


Figure 11. Repeatability error of reconstructions using method  $M_f$ .

point cloud challenging. A prerequisite for a valid comparison is a good alignment of the geometry. Rigid point-set registration is typically used for such alignment, we have used the Iterative Closest Point (ICP) algorithm (Chen & Medioni, 1992). Our experiments have proven that in order to have a well converging alignment, the ground truth point cloud needs to be processed to exclude the points that would be lost in reconstruction. When aligning two measurements produced by our method, this problem does not occur.

### 5. APPLICATION: TOOL WEAR MONITORING

The geometry reconstruction method presented in Section 3 provides the foundation for a cutting tool wear detection method. By comparing the geometry of a measurement at the beginning of the cutting tool’s life with measurements after use, the tool wear can be spatially visualized and quantified. This kind of analysis enables an expert to assess the severity of the tool wear, and take appropriate actions. A simple automated replacement method can be obtained by comparing the quantified tool wear to a threshold.

For alignment of two measurements the ICP algorithm is used, as presented in Section 4. For this purpose the entire point clouds of both measurements can be used. After alignment of the geometry, cutting tool wear can be quantified by a Euclidean distance metric. As a tool wear metric, we use point-to-closest-triangle distance between the triangular surface of the original measurement and the point cloud of the worn cutting tool measurement. These per-vertex values can be put in a histogram and compared to the point-to-closest-triangle repeatability histogram. This is a fair comparison if the vertices are distributed uniformly over the surfaces. However, the geometry coming out of our reconstruction does not exhibit this property. Indeed, there are more points in the curved areas, because there are more line scans associated with these areas. To account for this imbalance, weighted histograms can be of use. Each vertex is weighted by its local area:

$$w_i = \sum_{j \in T_i} A_j / 3$$

where,  $T_i$  are the neighbouring triangles of vertex  $i$  and  $A_j$  is the triangle area of triangle  $j$ . A weighted histogram then aggregates weight values by sum in each bin, instead of by count. Tool wear can now be assessed using an area weighted histogram of the point-to-closest-triangle distance. See Figure 12 (Appendix) for an illustration of such weighted histogram.

To validate our method with respect to tool wear detection, we have done accelerated degradation tests on drilling tools. In order to obtain wear quickly, a hard work piece material (stainless steel) and wrong cutting parameters were used on low cost tools. A quantitative and qualitative overview is given in Figure 13 (Appendix): the first row visualizes

the tool wear metric localized on the worn tool reconstruction, the point cloud of the original geometry is visualized in black; the second row displays the worn geometry with specular shading enabled in order to give a qualitative comparison of the cutting edge. Therefore the bottom row is rotated 90 degrees counter-clockwise. The tool wear metric is also presented in weighted histogram form in Figure 12. For illustrative purposes the degradation is driven to an unusable level. However, it is clear how the progression of wear can be seen in all three visualization forms. In Figure 13, most notably the corner point of the flank face has worn off after three holes and the chisel edge becomes smaller after each hole. The bottom row reveals how the initially sharp cutting edge has been chamfered and is blunt after two holes. In Figure 12 this progression of tool wear is also reflected. The first weighted histogram illustrates the repeatability in terms of point-to-triangle-distance. Subsequent histograms show a widening that corresponds to tool wear progression. Negative values are most indicative for tool wear. Positive values are present because of imperfect alignment of the non matching geometries. A simple quantification of the total tool wear considers the sum of the weights of the bins with magnitude above a certain threshold. This value can be used to trigger maintenance actions. This experiment validates our approach towards tool wear analysis using the proposed reconstruction method. It proves feasibility of the reconstruction method for tool wear monitoring, with moderate costs and off-the-shelf components.

Further efforts can investigate robust estimation methods in contaminated environments: cutting oil, coolant, chips, milling waste. Figure 12 also motivates investigation of the use of maximum curvature as a tool wear parameter.

## 6. CONCLUSION

In this article we presented a method for surface reconstruction of rotating geometry. By leveraging shadow traces of a spinning tool, the 2D convex hull of the geometry can be reconstructed. The accuracy of the proposed method proves sufficient for detecting tool wear. We compared two methods for shadow width estimation and see comparable performances when applying our adaptive threshold method  $M_a$  or our fixed threshold method  $M_f$  with respect to reconstruction quality, while the repeatability shows less variance when using the fixed threshold method  $M_f$ . When considering the Mean Absolute Errors in Table 1 with values around  $70 \mu m$  we attain values better than the accuracy possible by human visual inspection and the industry standard of  $100 \mu m$ . The results from our repeatability analysis with mean errors as low as around  $10 \mu m$  and the tool wear experiment results from Section 5 corroborate the feasibility of our approach for tool wear monitoring. The difference in distance distribution due to increasing wear is easily visible and traceable. Moreover, due to the low-cost set-up with autarkic equip-

ment, retro-fitting represents a viable way of transforming a conventional machining center into a smart one.

## ACKNOWLEDGEMENT

This research was supported by Flanders Make, the strategic research centre for the manufacturing industry. This work has also been supported by the COMET-K2 Center of the Linz Center of Mechatronics (LCM) funded by the Austrian federal government and the federal state of Upper Austria. The authors would like to thank Stijn Helsen for his efforts on the optical setup and data acquisition.

## REFERENCES

- Bagga, P., Makhesana, M., Patel, K., & Patel, K. (2021). Tool wear monitoring in turning using image processing techniques. *Materials Today: Proceedings*, 44, 771–775.
- Bey-Temsamani, A., Ooijejaar, T., & Depraetere, B. (2019). An assessment of two technologies for high performance composite machining; adaptive fixturing and in process tool profile monitoring. *Procedia CIRP*, 85, 201-206. Retrieved from <https://www.sciencedirect.com/science/article/pii/S2212827119312831> (2nd CIRP Conference on Composite Material Parts Manufacturing, 10-11 October 2019, Advanced Manufacturing Research Centre, UK) doi: <https://doi.org/10.1016/j.procir.2019.09.023>
- Bremner, D., Fukuda, K., & Marzetta, A. (1998, Oct 01). Primal—dual methods for vertex and facet enumeration. *Discrete & Computational Geometry*, 20(3), 333-357. Retrieved from <https://doi.org/10.1007/PL00009389> doi: 10.1007/PL00009389
- Chen, Y., & Medioni, G. (1992). Object modelling by registration of multiple range images. *Image and Vision Computing*, 10(3), 145-155. Retrieved from <https://www.sciencedirect.com/science/article/pii/026288569290066C> (Range Image Understanding) doi: [https://doi.org/10.1016/0262-8856\(92\)90066-C](https://doi.org/10.1016/0262-8856(92)90066-C)
- Krishnakumar, P., Rameshkumar, K., & Ramachandran, K. (2018). Feature level fusion of vibration and acoustic emission signals in tool condition monitoring using machine learning classifiers. *International Journal of Prognostics and Health Management*, 9(1).
- Kuntoğlu, M., Aslan, A., Pimenov, D. Y., Usca, Ü. A., Salur, E., Gupta, M. K., ... Sharma, S. (2020). A review of indirect tool condition monitoring systems and decision-making methods in turning: Critical analysis and trends. *Sensors*, 21(1), 108.
- Lo, S. H. (1985). A new mesh generation scheme for arbitrary planar domains. *International Journal for Numerical*

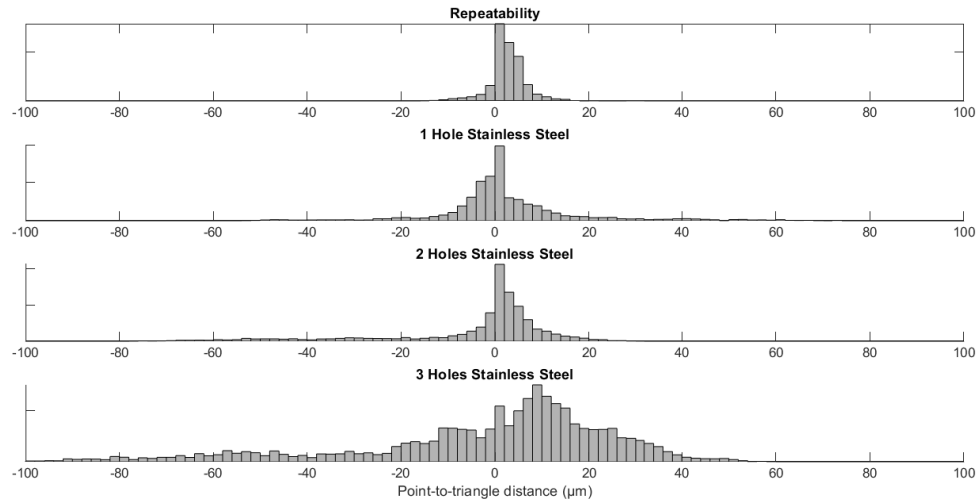


Figure 12. Progression of the weighted point-to-triangle distance histograms of a worn drill.

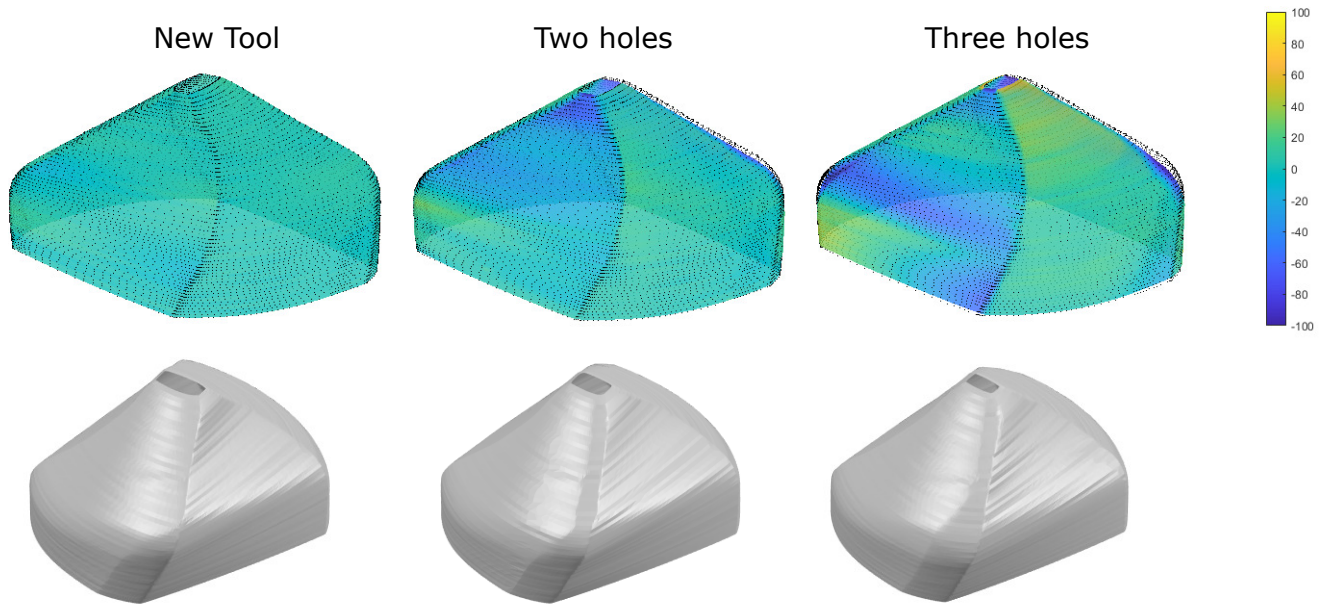


Figure 13. Visualized tool wear metric and shaded reconstructions of a (accelerated) degrading drilling tool. Left: unused drill; Middle: two holes in stainless steel; Right: three holes in stainless steel.

*Methods in Engineering*, 21(8), 1403-1426. Retrieved from <https://onlinelibrary.wiley.com/doi/abs/10.1002/nme.1620210805> doi: <https://doi.org/10.1002/nme.1620210805>

Peng, R., Pang, H., Jiang, H., & Hu, Y. (2020). Study of tool wear monitoring using machine vision. *Automatic Control and Computer Sciences*, 54(3), 259–270.

Zhu, K., & Zhang, Y. (2019). A generic tool wear model and its application to force modeling and wear monitoring in high speed milling. *Mechanical Systems and Signal*

*Processing*, 115, 147–161.

Čerče, L., Pušavec, F., & Kopač, J. (2015). A new approach to spatial tool wear analysis and monitoring. *Strojniški vestnik - Journal of Mechanical Engineering*, 61(9), 489-497. Retrieved from <https://www.sv-jme.eu/article/a-new-approach-to-spatial-tool-wear-analysis-and-monitoring/> doi: 10.5545/sv-jme.2015.2512